Acta Materialia 170 (2019) 132–137

Contents lists available at ScienceDirect

Acta Materialia

journal homepage: www.elsevier.com/locate/actamat

Full length article

Effect of single point defect on local properties in $BiFeO_3$ thin film

Xiaomei Li [a, e, 1], Mingqiang Li [b, c, 1], Xuanyi Li [a, e, 1], Shilu Tian [a, e], Adeel Y. Abid [b, c], Ning Li [b, c], Jianlin Wang [a, e], Lei Zhang [a], Xujing Li [a, b], Yanchong Zhao [a, e], Can Wang [a], Zhi Xu [a], Sheng Meng [a, d, **], Peng Gao [b, c, d, *], Xuedong Bai [a, d, ***]

[a] Beijing National Laboratory for Condensed Matter Physics and Institute of Physics, Chinese Academy of Sciences, Beijing, 100190, China
[b] Electron Microscope Laboratory, School of Physics, Peking University, Beijing, 100871, China
[c] International Center for Quantum Materials, School of Physics, Peking University, Beijing, 100871, China
[d] Collaborative Innovation Centre of Quantum Matter, Beijing, 100871, China
[e] University of Chinese Academy of Sciences, Beijing, 100049, China

ARTICLE INFO

Article history:
Received 10 January 2019
Received in revised form
16 March 2019
Accepted 21 March 2019
Available online 23 March 2019

Keywords:
Ferroelectric
Point defect
Scanning transmission electron microscopy
Quantitative image analysis
Density function calculations

ABSTRACT

Point defects commonly exist in artificially prepared ferroelectric oxide films. Here, the local polarization characteristics around a single point defect of Bi substitution in the Fe sites (antisite Bi, Bi_{Fe}) in $BiFeO_3$ (BFO) thin film, are studied at an atomic scale. Both first-principles theory and atomically resolved scanning transmission electron microscopy images show that a single point defect expands the lattice (~2.4% in-plane direction and 0.8% along out-of-plane direction) but suppresses the surrounding polarization by more than ~27%. The suppression of polarization is due to the formation of a single unit cell of non-ferroelectric Bi_2O_3, across which the accumulation of polarization bound charge induces a strong depolarization field. Therefore, structure relaxation makes the Bi_2O_3 coherently polarized and meanwhile suppresses the surrounding polarization. Such point defects act as a pinning center to domain wall motion, which gives rise to incomplete switching, fatigue, and aging of ferroelectric devices.

1. Introduction

Ferroelectric materials are widely used in electronic [1–3], optical [4], and piezoelectric devices [5]. Most of these applications require the ability of reversible polarization switching that is generally realized by the domain wall motion [1,6–8]. Defects that inevitably exist in these crystallographic ferroelectric materials dominate the switching behavior [6,8,9]. For example, previous studies showed that domain nucleation always started from the interface between the electrode and ferroelectrics [6,8], the ferroelastic domains and dislocations can weakly pin the domain wall motion [6,7], while the point defects may strongly hinder the domain wall movement to form unswitchable "interfacial domain" [8]. The defect structure dependent on ferroelectric switching behavior can be understood by the polarization bound charge screening mechanism [10,11]. Specifically, at the defects, the broken continuity of polar vectors causes an accumulation of polarization bound charge which requires either structural relaxation or redistribution of free carriers in order to minimize the depolarization field otherwise destabilizing the ferroelectric phase [10–13]. Note that for different types of defects, mechanical boundary conditions (e.g., strain, strain gradient) and electrical boundary conditions (e.g., stoichiometry, ionic and electronic doping) are different. In this sense, the boundary conditions of defects determine the compensation mechanism of polarization bound charge and further govern the switching behavior. Therefore, in order to understand the defects dominated switching behavior in ferroelectric devices, it is prerequisite to investigate atomic structure and chemistry of individual defects and its effect on the local properties such as polarization distribution (screen mechanisms).

The quantitative image analysis based on the aberration corrected transmission electron microscopy allows us to precisely measure the strain field, octahedral distortion, and polarization

* Corresponding author. Electron Microscope Laboratory, School of Physics, Peking University, Beijing, 100871, China.
** Corresponding author. Beijing National Laboratory for Condensed Matter Physics and Institute of Physics, Chinese Academy of Sciences, Beijing, 100190, China.
*** Corresponding author. Beijing National Laboratory for Condensed Matter Physics and Institute of Physics, Chinese Academy of Sciences, Beijing, 100190, China.
E-mail addresses: smeng@iphy.ac.cn (S. Meng), p-gao@pku.edu.cn (P. Gao), xdbai@iphy.ac.cn (X. Bai).
[1] These authors contributed equally to this work.

https://doi.org/10.1016/j.actamat.2019.03.028
1359-6454/

distribution around individual defect in ferroelectrics. For instance, it was reported that suppression of polarization occurs at the surface [13,14] and interface of ferroelectric/electrode [12,14,15], while enhancement of polarization was also observed at heterointerface of ferroelectric/ferroelectric [16]. The interfacial misfit dislocations suppress the surrounding polarization [17], weakly pin 180° domain walls motion [6], but strongly hinder the ferroelastic domain walls movement [18]. Even if the dislocation locates in the substrate [19], the influence would extend across the interface into the ferroelectric layer and reduce the c-lattice parameter and spontaneous polarization [15]. Recently, the second nanoscale nonstoichiometric phase in BFO showed exotic polarization rotation due to the presence of charge states [20]. The point defects also commonly exist in ferroelectrics particularly in the ferroelectric thin films made by molecular beam epitaxy (MBE) [8]. These zero-dimensional crystal defects naturally carry charges, which are expected to have interactions with domain walls via strong charge-charge interactions [8]. Particularly during polarization switching under external electrical fields, since the domain wall configuration commonly deviates from the equilibrium position to form charged domain wall [6,8], stronger interaction occurs and may completely hinder the domain wall motion [8]. However, it is very tedious to identify the point defects due to their single-atom size [9], leaving the properties of point defects and the interactions with domain walls largely unknown [8].

Here, we combine the density functional theory (DFT) with atomically resolved Z-contrast image in scanning transmission electron microscopy (STEM) to study the influential role of individual point defect of Bi substitution in the Fe sites (antisite Bi, Bi_{Fe}) in an epitaxial bilayer of BFO on $La_{0.7}Sr_{0.3}MnO_3$ (LSMO) electrode. We find that point defects are formed by the substitution of Bi atoms into the Fe sites, along with >37% reduction in polarization in the region adjacent to the point defect. The experimental observations are in excellent agreement with theoretical calculations. The reduction of polarization is due to the broken continuity of polar vectors across the point defect where the depolarization field drives the surrounding BFO to relax and thus alters the adjacent polarization. The point defect has strong interactions with domain walls acting as the pinning center to domain wall motion, which mainly accounts for the incomplete switching, fatigue, and aging of ferroelectric devices. This study reveals the atomic-scale polarization distribution near a single point defect, providing valuable insights into understanding the failure mechanism of ferroelectric devices.

2. Experimental and calculational methods

The 50 nm-thick BFO thin films with 20 nm-thick LSMO layer as bottom electrode were epitaxially grown on TiO_2-terminated (001) $SrTiO_3$ (STO) single crystal substrates using laser molecule beam epitaxy system (Laser-MBE). A XeCl excimer laser with wavelength of 308 nm was used with an energy density of around 1.5 J/cm^2 and a repetition of 2 Hz. The STO substrates were etched by buffered HF and annealed in flowing oxygen to get the atomic-flat TiO_2-terminated surface. During the growth of BFO layer, the substrate was kept at 630 °C, and the oxygen pressure in the chamber was 15 Pa. Before the growth of BFO layer, a 20 nm-thick LSMO layer was deposited at 800 °C and 30 Pa.

Cross-sectional TEM specimens were prepared by mechanical polishing followed by argon ion milling in Precision Ion Polishing System 691 (Gatan). Ion milling procedure consists of two steps. At the first stage of coarse milling, the guns were set at 4 keV with angles 5° and −5°. In the following conditions, the guns were set at 1 keV for 5 min with angles of 3.5° and −3.5°, and further lowered to 0.1 keV for 2 min for final surface cleaning. Atomic resolution scanning TEM images were acquired using the FEI Titan Themis G2 operated at 300 kV. The convergence semiangle for imaging is 21.5 mrad, and the collection semi-angles snap is 48–200 mrad for the high angle annular dark field (HAADF) image. The beam current is ~70 pA. The HAADF image is simulated by using the software COMPUTEM described by Kirkland [21].

Atom positions in the HAADF images are determined by simultaneously fitting with two-dimensional Gaussian peaks to a priori perovskite unit cell using a MatLab code [22]. Both the atomic displacements and lattice constants are calculated based on the atom positions. The spontaneous polarization for this thin film can be calculated by measuring the relative displacements based on the previous studies on Born effective charge method [23]. Displacement vectors of the A column were measured relative to the center of the surrounding B columns in the HAADF images, where A and B can be Bi and Fe columns. Local ferroelectric polarization P_S is proportional to D_{FB} as $P_S \propto \pm D_{FB}$, and the relative displacement of the Fe atom is in the opposite direction of the polarization [24], whereas for Bi atom it is in the same direction of the polarization [3,25].

The first-principles calculations were performed with the projector-augmented wave (PAW) [26] pseudopotentials implemented in Vienna Ab initio Simulation Package (VASP) [27]. We used the generalized gradient approximation (GGA) [23] form of exchange-correction functional to perform electronic structure calculations and geometry optimization. A plane wave basis set with a 400 eV kinetic energy cutoff is adopted. The structures are considered to be fully relaxed until the total energy between sequential ionic steps is less than 0.1 meV and the Hellmann-Feynman force on each atom is less than 0.01 eV/Å.

3. Results and discussions

We first investigate the potential effects of a single Bi_{Fe} defect on the properties of BFO by quantum mechanical DFT calculations. Two supercells are constructed, comprising $4 \times 4 \times 2$ cells of BFO primitive cell of the trigonal system. In one of the supercells we replace a Fe atom with Bi atom in the middle of the super cell as substitution (Fig. 1(a)), and the other is perfect $4 \times 4 \times 2$ cells of BFO primitive cell as a reference. For the DFT study of these geometrical models, self-consistent calculations would stop only when all of the atoms are fully relaxed and the system reaches the lowest energy. Based on the previous studies [23], the spontaneous polarization for BFO can be calculated by measuring the relative displacements of each atoms D_{FB} with respect to the center of four surrounding atoms [28,29]. Positions of Bi atoms represent positive centers and positions of Fe atoms represent the negative center because each Fe atom is the center of the ferrite octahedron. With accurate atom coordinates, we calculate the distance between the positive and negative charge centers, and then the electric dipole moment, to calibrate the local polarization. The calculated polarization (Fig. 1(b)) map shows that the polarization decreases to ~47.5 μC/cm^2 in the substitution site, nearly 37% smaller than that in the reference super cell (~75.8 μC/cm^2).

In Fig. 2(a), a HAADF image of a point defect is also simulated on the basis of a large cell consisting of one substituted and nineteen normal cells stacking together along c axis. This simulated Z-contrast image (Z is the atomic number) further depicts that each high-intensity Bi cation is surrounded by four low-intensity Fe cations representing the projected perovskite unit cells of the rhombohedral BFO, whereas lighter oxygen, however, is invisible due to the weak scattering at high angles. Another striking structural feature is that the central Fe column is much brighter than that of the others due to the substitution a heavy Bi atom, which is also confirmed by the right-side intensity profile corresponding to

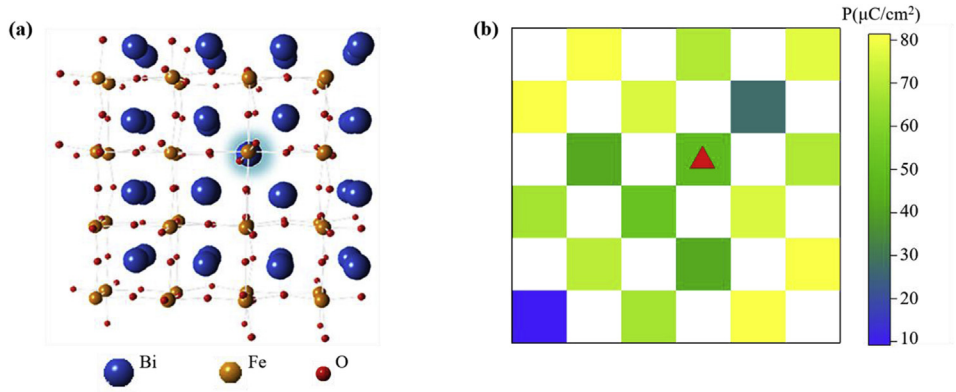

Fig. 1. Simulated polarization distribution for a single point defect Bi_{Fe} in $BiFeO_3$ (BFO). (a) An atomistic mode of a point defect Bi_{Fe}. (b) The corresponding two-dimensional (2D) displacement map between Bi and Fe atoms. Every color foursquare parallelism corresponds to a cation column in the left image. The red triangle highlights the location of point defect. (For interpretation of the references to color in this figure legend, the reader is referred to the Web version of this article.)

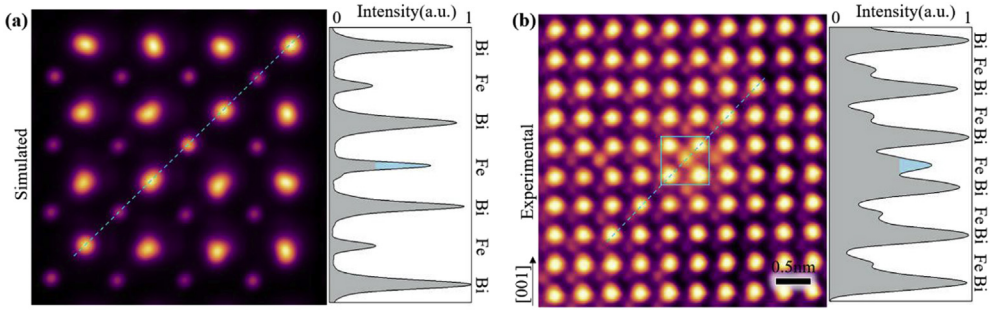

Fig. 2. Simulated and experimental observation of a point defect Bi_{Fe}. (a) Simulated image of an area contains a point defect Bi_{Fe}. The intensity profile at right corresponds to the dashed line in the image. (b) Experimental Z-contrast image of an area contains a point defect Bi_{Fe}. The right line intensity profile corresponds to the dashed blue line. (For interpretation of the references to color in this figure legend, the reader is referred to the Web version of this article.)

dash blue line.

Experimentally identifying the substitional Bi_{Fe} defect and measuring the surrounding polarization is a great challenge because the single atom sized point defect buried inside the crystal is usually invisible for most of characterization techniques. A HAADF image viewed along the [100] direction of the BFO thin film in Fig. 2(b) shows a point defect. The thickness of epitaxial BFO thin films is 50 nm with 20 nm LSMO buffered electrodes grown on (001) $SrTiO_3$ single crystal substrates by pulsed-laser deposition. During film-growth, we have not introduced any other elements. In addition, the contrast of the point defect in the Z-contrast image in Fig. 2 shows that the experimental contrast is in good agreement with simulation. Thus, the bright atom in the Fe sites should be Bi, i.e., substitution of a heavy element Bi into the Fe site. Therefore, this defective unit cell turns out to be Bi_2O_3. The formation of the Bi_2O_3 was related to the film growth process, which has no connection with the BFO decomposition [30,31]. Due to the clamp effect from the surrounding unit cells, the atomic structure of such defective unit cell does not change significantly except for the slight expansion of the lattice constant as shown in Fig. 3 and Fig. S1, i.e., the lattice constant of the point defect unit cell becomes larger, while the vicinity unit cell is smaller as confirmed by both experimental and theoretical investigations. With the expansion of the defective unit cell, oxygen octahedron occurs deformation and the distance between positive and negative centers becomes smaller, that is, the polarization is reduced. The lattice expansion at such a point defect can be understood by the much larger ionic radius of Bi^{3+} (1.17 Å) than that of Fe^{3+} (0.645 Å) [32]. We have measured many point defects Bi_{Fe} from different regions and all of them show the same trend of lattice changes as shown in Fig. 3. The formation energy of this defect is about − 6.451 eV, suggesting such defects could stably exist in the thin film [33–35].

Fig. 4(a) is the displacement map of a point defect and its surrounding vicinity [36]. Notably, the existence of point defect does not change the direction, but reduces the magnitude of surrounding displacement vectors. The magnitude of the displacement around the point defect is plotted atom by atom in Fig. 4(d), the displacement is smaller as compared to the rest of region, indicating suppression of polarization. At the point defect column, the magnitude $|D_{FB}|$ is reduced to ~0.471 Å, which is nearly 27% smaller than that of averaged value of ~0.653 Å for outermost layers. And other point defects in different regions show the same trend as shown in Fig. 4(b) (c) and (e) (f).

The suppression of surrounding polarization can be interpreted by the screening mechanism of polarization bound charge at the defects. Across the point defect, the broken continuity of polar vectors leads to the accumulation of polarization charge, which drives the surrounding BFO to relax to compensate the polarization charge otherwise the unscreened depolarization field destroys the ferroelectricity. Meanwhile the point defect itself, Bi_{Fe} that is a single unit cell of Bi_2O_3, is coherently polarized. The Bi_2O_3 is supposed to be non-ferroelectric. Along the polarization direction, polarization bound charge is opposite on the two sides of point defect. Thus, a strong electrical field is generated and applied to the single unit cell Bi_2O_3, driving the Bi away from the center, as the theoretical calculation suggested in Fig. 1. It can be also understood by a general symmetry-conforming property of point defects [37–40] that polar lattice defect aligns along spontaneous-

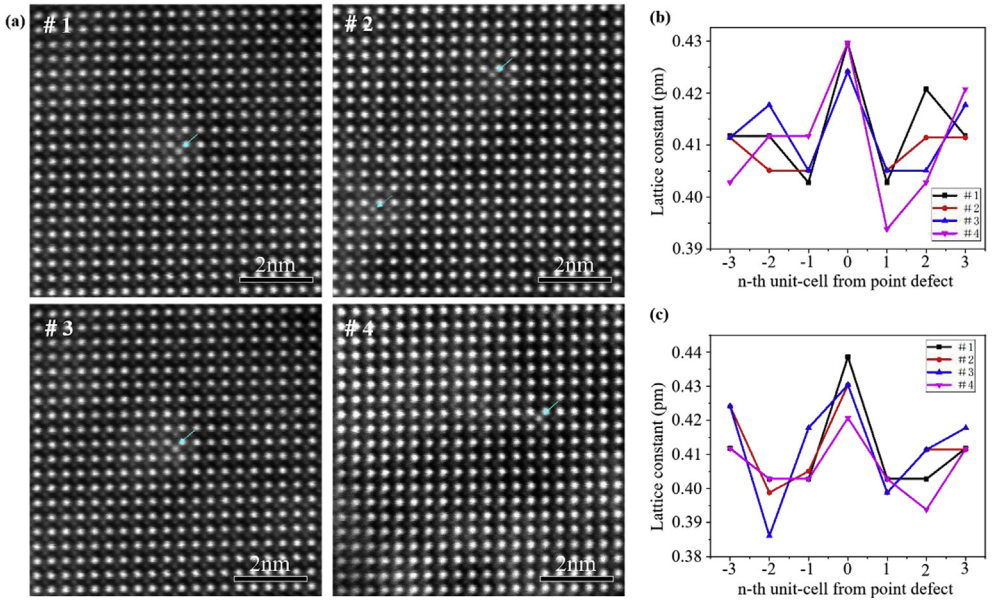

Fig. 3. The point defect Bi_{Fe} in the other regions of the same specimen and the lattice contant change. (a) The point defect Bi_{Fe} in the other regions of the same specimen. (b) Lattice constant change in the horizontal direction around the point defect. (c) Lattice constant change in the vertical direction around the point defect.

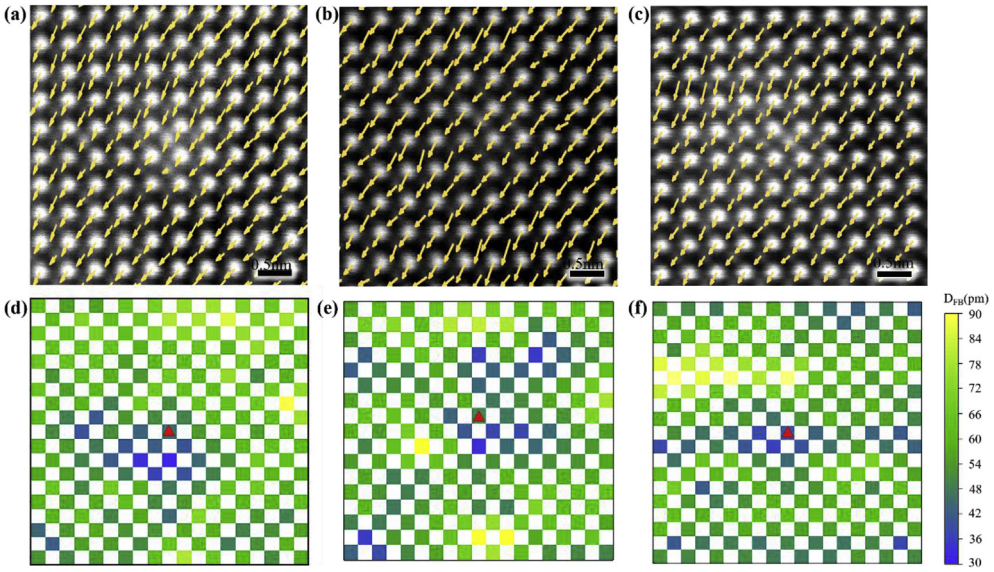

Fig. 4. Displacement map of a point defect region. (a) A Z-contrast image of Fig.2(b) overlaid with displacement vectors (shown by yellow arrows), $\mathbf{D}_{FB}$ vector. (b) and (c) Z-contrast images corresponding to the #1 and #2 overlaid with the displacement vectors (shown by yellow arrows), $\mathbf{D}_{FB}$ vector. Note that the magnitude around the point defect becomes smaller. (d) (e) and (f) The corresponding 2D displacement maps. Every color foursquare parallelism corresponds to a cation column in the left image. The red triangles highlight the locations of point defect. (For interpretation of the references to color in this figure legend, the reader is referred to the Web version of this article.)

polarization orientation and has the same symmetry with the neighbors.

The experimental results of polarization suppression (~27%) and coherently polarized point defect are basically in good agreement with the DFT calculations (~37%) except that the theoretically calculated polarization at the point defect is smaller than that of the experimentally measured values. Note that the contrast of an 'atom' in the HAADF image is determined by an atom column along the electron beam propagation direction rather than a single atom. For a Fe column containing a Bi_{Fe} point defect, the unit cell of the defect and neighbors along the electron beam direction has smaller displacement while those far away from defect remain unchanged. All these unit cells contribute together to the contrast of HAADF image. Therefore, the experimentally measured value is averaged from the reduced displacements around the point defect ('true' value) and normal case far away from the defect. In this sense, the suppression of polarization at the defect should be even more significant than that in Fig. 4 and therefore DFT calculation likely gives a better estimation of the true value.

Previous studies reported that after electrical switching a point defect, Bi_{Fe}, was observed at a negatively charged 180° domain-wall, indicating the strong pinning effect of such point defect on domain wall motion [8]. Similar pinning effect of point defect Bi_{Fe} on 109° domain wall is observed in this work. In the HAADF image over laid with the polarization direction color maps in Fig. 5 (see also Fig. 6), a point defect exists at an inclined (bent) 109° domain

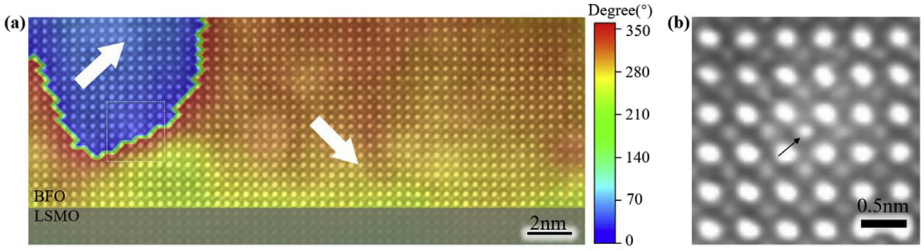

Fig. 5. A point defect at a 109° domain wall in BFO. (a) A Z-contrast image of a region containing a point defect at a negatively charge 109° domain wall. The large white arrows in the image label the polarization direction. The color corresponds to the polarization angle. The unit of color is degree. (b) The enlarged view of Z-contrast image corresponding to the region of white frame in the (a) shows the point defect indicated by the black arrow. (For interpretation of the references to color in this figure legend, the reader is referred to the Web version of this article.)

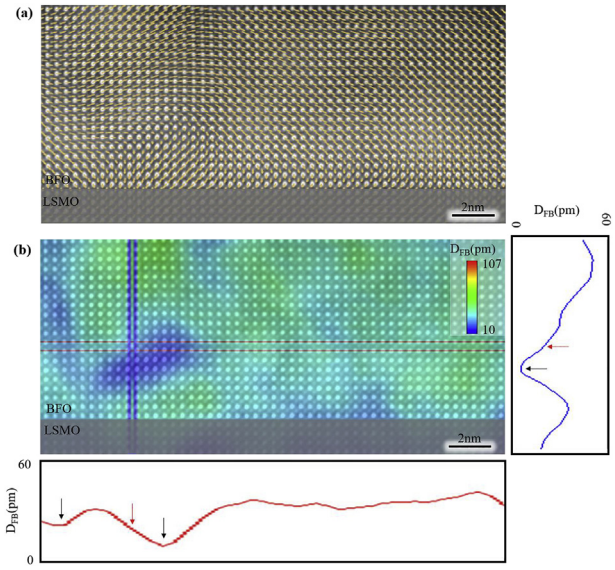

Fig. 6. The polarization map of a region with a point defect beside the 109° domain wall. (a) Spatial distribution of the displacement vectors overlaid on the HAADF STEM image. (b) The corresponding color maps of the magnitude of polarization. The color and its intensity represent the polarization magnitude. The below red line intensity profile corresponds to the highlighted red region, and the right blue line intensity profile corresponds to the blue region. (For interpretation of the references to color in this figure legend, the reader is referred to the Web version of this article.)

wall. From the first principles calculations [41,42], the 109° domain wall lying on {100} planes has the lowest energy. Therefore, this curved 109° domain wall must be negatively charged. It is reasonably concluded that the interactions between point defect and domain wall drag the 109° domain wall deviate from the equilibrium position to be bent. Such strong charge-charge interactions make the point defect a strong pinning center to 109° domain wall motion, similar to the strong pinning effect on 180° domain wall motion [8].

We also calculate the electronic structure of such defective BFO supercell. Compared to the perfect BFO cell (Fig. S2), when a Bi atom is substituted with a Fe atom, an extra band appears. This energy band, which appears close to the Fermi level, is contributed by the point defect Bi atom and its surrounding Fe and O atoms, as evidenced from local density of states (LDOS) calculations. Bader charge analysis [43] shows that the electrons are more dispersed in the surrounding oxygen octahedron, and those Fe atoms next to the point defect have lost more electrons. It also shows the decrease of charge density of Bi atoms along the polarization direction. This result is also in accordance with and provides further evidences to the decrease of polarization around the point defect. Charge density changes and redistributes because of the point defect, and the optical properties are also expected to change due to the formation of defective state.

In ferroelectric devices, the interaction between point defect and domain wall during electrical loading causes incomplete switching and influence the properties such as hysteresis loop [44], dielectric constant [45], piezoelectric constant change and cycling stability. In fact, the pinning effect of the point defect on domain wall motion is believed to be responsible for aging and fatigue in ferroelectric thin films and devices [46,47]. The aging and fatigue phenomena have been frequently observed in almost all ferroelectrics and are usually supposed to be detrimental.

4. Conclusion

In summary, our combined first principles calculations and quantitative image analysis clearly depict the existence of the Bi_{Fe} point defect and its significant impact on the properties of BFO. Both experiment and theoretical calculation confirm that the surrounding polarization of the defect is significantly suppressed, while the point defect itself is coherently polarized. The Bi substitution also causes lattice expansion. The suppression of polarization can be understood by the screening mechanisms, i.e., across the point defect the polarization bound charge drives the structure relaxation to minimize the depolarization field, leading to suppression of polarization. The same type of point defect is observed at a bent (charged) 109° domain wall, showing a strong interaction with the domain wall. The pinning effect of the point defects should be largely responsible for the aging and fatigue of ferroelectric devices. Our findings can help us to explain the past incomplete switching events in ferroelectric thin films, provide useful insights into understanding of aging and fatigue phenomena in ferroelectric devices, and open the door to manipulate the local polarization in the monatomic level through defect engineering.

Acknowledgements

The authors acknowledge the support from the National Equipment Program of China (ZDYZ2015-1), National Basic Research Program of China (2016YFA0300804 and 2016YFA0300903), National Natural Science Foundation of China (51672007, 51502007, 11327902 and 11474337), and the National Program for Thousand Young Talents of China.

Appendix A. Supplementary data

Supplementary data to this article can be found online at https://doi.org/10.1016/j.actamat.2019.03.028.

References

[1] M. Dawber, K.M. Rabe, J.F. Scott, Physics of thin-film ferroelectric oxides, Rev. Mod. Phys. 77 (4) (2005) 1083–1130.
[2] N. Setter, R. Waser, Electroceramic materials, Acta Mater. 48 (2000) 151.
[3] J. Scott, Applications of modern ferroelectrics, Science 315 (5814) (2007) 954–959.
[4] W.J. Hu, Z. Wang, W. Yu, T. Wu, Optically controlled electroresistance and electrically controlled photovoltage in ferroelectric tunnel junctions, Nat. Commun. 7 (2016) 10808.
[5] J.X. Zhang, B. Xiang, Q. He, J. Seidel, R.J. Zeches, P. Yu, S.Y. Yang, C.H. Wang, Y.H. Chu, L.W. Martin, A.M. Minor, R. Ramesh, Large field-induced strains in a lead-free piezoelectric material, Nat. Nanotechnol. 6 (2011) 98.
[6] P. Gao, C.T. Nelson, J.R. Jokisaari, S.H. Baek, C.W. Bark, Y. Zhang, E. Wang, D.G. Schlom, C.B. Eom, X. Pan, Revealing the role of defects in ferroelectric switching with atomic resolution, Nat. Commun. 2 (2011) 591.
[7] P. Gao, J. Britson, J.R. Jokisaari, C.T. Nelson, S.-H. Baek, Y. Wang, C.-B. Eom, L.-Q. Chen, X. Pan, Atomic-scale mechanisms of ferroelastic domain-wall-mediated ferroelectric switching, Nat. Commun. 4 (2013) 2791.
[8] C.T. Nelson, P. Gao, J.R. Jokisaari, C. Heikes, C. Adamo, A. Melville, S.H. Baek, C.M. Folkman, B. Winchester, Y. Gu, Y. Liu, K. Zhang, E. Wang, J. Li, L.Q. Chen, C.B. Eom, D.G. Schlom, X. Pan, Domain dynamics during ferroelectric switching, Science 334 (6058) (2011) 968–971.
[9] S.V. Kalinin, B.J. Rodriguez, A.Y. Borisevich, A.P. Baddorf, N. Balke, H.J. Chang, L.-Q. Chen, S. Choudhury, S. Jesse, P. Maksymovych, M.P. Nikiforov, S.J. Pennycook, Defect-mediated polarization switching in ferroelectrics and related materials: from mesoscopic mechanisms to atomistic control, Adv. Mater. 22 (3) (2010) 314–322.
[10] S. Hong, S.M. Nakhmanson, D.D. Fong, Screening mechanisms at polar oxide heterointerfaces, Rep. Prog. Phys. 79 (7) (2016), 076501.
[11] S.V. Kalinin, Y. Kim, D. Fong, A. Morozovska, Surface Screening Mechanisms in Ferroelectric Thin Films and its Effect on Polarization Dynamics and Domain Structures. 1612 (2016) 08266.
[12] P. Gao, Z. Zhang, M. Li, R. Ishikawa, B. Feng, H.-J. Liu, Y.-L. Huang, N. Shibata, X. Ma, S. Chen, Possible absence of critical thickness and size effect in ultrathin perovskite ferroelectric films, Nat. Commun. 8 (2017) 15549.
[13] P. Gao, H.J. Liu, Y.L. Huang, Y.H. Chu, R. Ishikawa, B. Feng, Y. Jiang, N. Shibata, E.G. Wang, Y. Ikuhara, Atomic mechanism of polarization-controlled surface reconstruction in ferroelectric thin films, Nat. Commun. 7 (2016) 11318.
[14] C.L. Jia, V. Nagarajan, J.Q. He, L. Houben, T. Zhao, R. Ramesh, K. Urban, R. Waser, Unit-cell scale mapping of ferroelectricity and tetragonality in epitaxial ultrathin ferroelectric films, Nat. Mater. 6 (1) (2007) 64–69.
[15] C.L. Jia, S.B. Mi, K. Urban, I. Vrejoiu, M. Alexe, D. Hesse, Effect of a single dislocation in a heterostructure layer on the local polarization of a ferroelectric layer, Phys. Rev. Lett. 102 (11) (2009) 117601.
[16] Y. Liu, Y.-L. Zhu, Y.-L. Tang, Y.-J. Wang, Y.-X. Jiang, Y.-B. Xu, B. Zhang, X.-L. Ma, Local enhancement of polarization at $PbTiO_3$/$BiFeO_3$ interfaces mediated by charge transfer, Nano Lett. 17 (6) (2017) 3619–3628.
[17] S.P. Alpay, I.B. Misirlioglu, V. Nagarajan, R. Ramesh, Can interface dislocations degrade ferroelectric properties? Appl. Phys. Lett. 85 (2004) 2044.
[18] P. Gao, J. Britson, C.T. Nelson, J.R. Jokisaari, C. Duan, M. Trassin, S.H. Baek, H. Guo, L. Li, Y. Wang, Y.H. Chu, A.M. Minor, C.B. Eom, R. Ramesh, L.Q. Chen, X. Pan, Ferroelastic domain switching dynamics under electrical and mechanical excitations, Nat. Commun. 5 (2014) 3801.
[19] C.L. Jia, A. Thust, K. Urban, Atomic-scale analysis of the oxygen configuration at a $SrTiO_3$ dislocation core, Phys. Rev. Lett. 95 (22) (2005) 225506.
[20] L. Li, X. Cheng, J.R. Jokisaari, P. Gao, J. Britson, C. Adamo, C. Heikes, D.G. Schlom, L.-Q. Chen, X. Pan, Defect-induced hedgehog polarization states in multiferroics, Phys. Rev. Lett. 120 (13) (2018) 137602.
[21] E.J. Kirkland, Advanced Computing in Electron Microscopy, Plenum Press New Yock, 1998.
[22] C.T. Nelson, B. Winchester, Y. Zhang, S.J. Kim, A. Melville, C. Adamo, C.M. Folkman, S.H. Baek, C.B. Eom, D.G. Schlom, L.Q. Chen, X. Pan, Spontaneous vortex nanodomain arrays at ferroelectric heterointerfaces, Nano Lett. 11 (2) (2011) 828–834.
[23] X. Gonze, C. Lee, Dynamical matrices, Born effective charges, dielectric permittivity tensors, and interatomic force constants from density-functional perturbation theory, Phys. Rev. B 55 (16) (1997) 10355–10368.
[24] L. Li, Y. Zhang, L. Xie, J.E. Jokisaari, C. Beekman, J.-C. Yang, Y.-H. Chu, H.M. Christen, X. Pan, Atomic-scale mechanisms of defect-induced retention failure in ferroelectrics, Nano Lett. 17 (2017) 3556–3562.
[25] V. Garcia, S. Fusil, K. Bouzehouane, S. Enouz-Vedrenne, N.D. Mathur, A. Barthelemy, M. Bibes, Giant tunnel electroresistance for non-destructive readout of ferroelectric states, Nature (London) 460 (7251) (2009) 81.
[26] W. Zhong, R. King-Smith, D. Vanderbilt, Giant LO-TO splittings in perovskite ferroelectrics, Phys. Rev. Lett. 72 (22) (1994) 3618.
[27] G. Kresse, J. Hafner, Ab initio molecular dynamics for liquid metals, Phys. Rev. B 47 (1) (1993) 558.
[28] P. Maksymovych, S. Jesse, P. Yu, R. Ramesh, A.P. Baddorf, S.V. Kalinin, Polarization control of electron tunneling into ferroelectric surfaces, Science 324 (5933) (2009) 1421–1425.
[29] J.F. Scott, C.A.P. De Araujo, Ferroelectric memories, Science 246 (4936) (1989) 1400–1405.
[30] E. Heifets, E.A. Kotomin, A.A. Bagaturyants, J. Maier, Thermodynamic stability of stoichiometric $LaFeO_3$ and $BiFeO_3$: a hybrid DFT study, Phys. Chem. Chem. Phys. 19 (2017) 3738–3755.
[31] E. Heifets, E.A. Kotomin, A.A. Bagaturyants, J. Maier, Thermodynamic stability of non-stoichiometric $SrFeO_{3-\delta}$: a hybrid DFT study, Phys. Chem. Chem. Phys. 21 (2019) 3918.
[32] X. Wang, G. Hu, L. Cheng, C. Yang, W. Wu, Comparative study on aging effect in BiFeO3 thin films substituted at A-and B-sites, Appl. Phys. Lett. 99 (26) (2011) 262901.
[33] E.A. Kotomin, Y.A. Mastrikov, M.M. Kuklja, R. Merkle, A. Roytburd, J. Maier, First principles calculations of oxygen vacancy formation and migration in mixed conducting $Ba_{0.5}Sr_{0.5}Co_{1-y}Fe_yO_{3-\delta}$ perovskites, Solid State Ionics 188 (1) (2011) 1–5.
[34] M.M. Kuklja, Y.A. Mastrikov, B. Jansang, E.A. Kotomin, The intrinsic defects, disordering, and structural stability of $Ba_xSr_{1-x}Co_yFe_{1-y}O_{3-\delta}$ perovskite solid solutions, J. Phys. Chem. C 116 (35) (2012) 18605–18611.
[35] A. Jain, S.P. Ong, G. Hautier, W. Chen, W.D. Richards, S. Dacek, S. Cholia, D. Gunter, D. Skinner, G. Ceder, K.A. Persson, The materials project: a materials genome approach to accelerating naterials innovation, Apl. Mater. 1 (1) (2013), 011002.
[36] C.T. Nelson, P. Gao, J.R. Jokisaari, C. Heikes, C. Adamo, A. Melville, S.H. Baek, C.M. Folkman, B. Winchester, Y. Gu, Y. Liu, K. Zhang, E. Wang, J. Li, L.Q. Chen, C.B. Eom, D.G. Schlom, X. Pan, Spontaneous vortex nanodomain arrays at ferroelectric heterointerfaces, Nano Lett. 11 (2) (2011) 828–834.
[37] X. Ren, Large electric-field-induced strain in ferroelectric crystals by point-defect-mediated reversible domain switching, Nat. Mater. 3 (2) (2004) 91.
[38] L. Zhang, W. Chen, X. Ren, Large recoverable electrostrain in Mn-doped (Ba, Sr)TiO_3 ceramics, Appl. Phys. Lett. 85 (23) (2004) 5658–5660.
[39] L.X. Zhang, X. Ren, In situ observation of reversible domain switching in aged Mn-doped $BaTiO_3$ single crystals, Physiol. Rev. B 71 (17) (2005) 174108.
[40] X. Ren, K. Otsuka, Origin of rubber-like behaviour in metal alloys, Nature 389 (6651) (1997) 579.
[41] O. Diéguez, P. Aguado-Puente, J. Junquera, J. Íñiguez, Domain walls in a perovskite oxide with two primary structural order parameters: first-principles study of $BiFeO_3$, Phys. Rev. B 87 (2) (2013), 024102.
[42] Y. Wang, C. Nelson, A. Melville, B. Winchester, S. Shang, Z.-K. Liu, D.G. Schlom, X. Pan, L.-Q. Chen, $BiFeO_3$ Domain wall energies and structures: a combined experimental and density functional theory +U study, Phys. Rev. Lett. 110 (26) (2013) 267601.
[43] E. Sanville, S.D. Kenny, R. Smith, G. Henkelman, Improved grid-based algorithm for Bader charge allocation, J. Comput. Chem. 28 (5) (2010) 899–908.
[44] S.V. Kalinin, S. Jesse, B.J. Rodriguez, Y.H. Chu, R. Ramesh, E.A. Eliseev, A.N. Morozovska, Probing the role of single defects on the thermodynamics of electric-field induced phase transitions, Phys. Rev. Lett. 100 (15) (2008) 155703.
[45] C. Canedy, H. Li, S. Alpay, L. Salamanca-Riba, A. Roytburd, R. Ramesh, Dielectric properties in heteroepitaxial $Ba_{0.6}Sr_{0.4}TiO_3$ thin films: effect of internal stresses and dislocation-type defects, Appl. Phys. Lett. 77 (11) (2000) 1695–1697.
[46] Y.A. Genenko, J. Glaum, M.J. Hoffmann, K. Albe, Mechanisms of aging and fatigue in ferroelectrics, Mater. Sci. Eng. B 192 (2015) 52–82.
[47] P.V. Lambeck, G.H. Jonker, The nature of domain stabilization in ferroelectric perovskites, J. Phys. Chem. Solids 47 (5) (1986) 453–461.